AS 3631
pp: 1-19 (col.fig.: Nil)

PROD. TYPE: COM

ED: S. Latha
PAGN: VD – SCAN: Radhika

ARTICLE IN PRESS

ELSEVIER

Aerosol Science ▮▮▮ (▮▮▮▮) ▮▮▮–▮▮▮

Journal of
Aerosol Science

www.elsevier.com/locate/jaerosci

Formation of charged soot aggregates by combustion and pyrolysis: charge distribution and photophoresis

V.V. Karasev[a], N.A. Ivanova[a], A.R. Sadykova[a], N. Kukhareva[a], A.M. Baklanov[a], A.A. Onischuk[a,*], F.D. Kovalev[b], S.A. Beresnev[b]

[a] *Institute of Chemical Kinetics and Combustion, Siberian Branch of the Russian Academy of Sciences, Novosibirsk 630090, Russia*

[b] *Aerosol Physics Laboratory, Physics Department, Ural State University, Ekaterinburg 620083, Russia*

Received 1 July 2003; accepted 18 September 2003

Abstract

Soot aggregates formed by propane combustion in a diffusion flame and benzene pyrolysis in a flow reactor are studied by a microscopic video system (at standard temperature and pressure) and transmission electron microscope. The radius of soot aggregates is in the range 0.1–1.0 μm. The size of primary particles in aggregates is 10–30 nm for the combustion aggregates and 40–200 nm for the pyrolysis aggregates. By video observations of aggregate movement in the electric field it is determined that soot aggregates are charged. The typical aggregate charge is a few elementary units. The soot charge distribution is roughly bipolar and symmetric. This charge distribution is governed by the Boltzmann law with the charging equivalent diameter d_E being larger than the aggregate mean mobility diameter by a factor of 1.4, 3.0 and 1.8 for soots sampled from the flame axis, region over the flame and from the flow reactor, respectively.

Photophoretic movement of soot aggregates driven by a helium–neon laser beam (3 W/cm^2) is observed by the video system. The aggregate photophoretic velocity is determined to be increasing from 15 to 160 μm/s with the equivalent radius increasing from 0.1 to 2.9 μm. Estimations of the sun photophoretic velocity V_{Ph}^{Sun} (in the Earth's atmosphere at ground level) indicate that it is about 20% of the settling velocity for the range of aggregate radii studied in this work. The velocities of soot aggregate photophoresis in the Earth thermal irradiation were estimated to be negligible with regard to the settling velocity.

Keywords: Soot particles; Charge distributions; Photophoresis

* Corresponding author. Tel.: +73-83-233-1322; fax: +73-83-234-2350.
E-mail address: onischuk@ns.kinetics.nsc.ru (A.A. Onischuk).

0021-8502/$ - see front matter © 2003 Published by Elsevier Ltd.
doi:10.1016/j.jaerosci.2003.10.006

Nomenclature

C_C	Cunningham correction factor
D	aggregate diffusion coefficient
D_f	fractal-like dimension
d_E	charging equivalent diameter
E	electric field strength
e	elementary charge (4.8×10^{-10} units of CGSE)
F_D	drag force
F_{Ph}^{agg}	photophoretic force acting to the aggregate
F_{Ph}^{single}	photophoretic force acting to a single spherical particle of radius r
F_{Ph}^{Sun}	sun photophoretic force
$f(q)$	charge distribution function
f_1	input flow rate in the benzene pyrolysis reactor
f_2	nitrogen dilution flow rate in the benzene pyrolysis reactor
f_3	air dilution flow rate in the benzene pyrolysis reactor
g	acceleration due to gravity
I	intensity of light (erg cm^{-2} s^{-2})
J_1	photophoretic asymmetry factor
k	imaginary part of refractive index
k_B	Boltzmann constant ($k_B = 1.38066 \times 10^{-23}$ J/K)
k_p	benzene pyrolysis rate constant
$Kn = \lambda/r$	Knudsen number
m	mass of gas molecules
M	aggregate mass
n_c	charge number of the aggregate
n	real part of refractive index
$q = n_c e$	aggregate charge
p_0	ambient gas pressure
r	radius of a single particle
$R\left(=\frac{1}{2}\sqrt{LW}\right)$	aggregate radius determined by transmission electron microscopy images, L and W are the length and width of the smallest rectangle enclosing the aggregate's image
R_a	equivalent projected area radius
R_m	mobility equivalent radius of aggregate
T	temperature
t	reaction time
v	aggregate velocity
v_{settl}	aggregate settling velocity
V_{Ph}^{single}	photophoretic velocity of single particle
V_{Ph}^{Sun}	sun photophoretic velocity
$[C_6H_6]$	benzene concentration at the reactor outlet
$[C_6H_6]_0$	benzene concentration at the reactor inlet

ξ	benzene decomposition degree
λ	gas mean free path
η	viscosity coefficient
χ_a	coefficient of thermal conductivity for gas
χ_i	coefficient of thermal conductivity for material of particle

1. Introduction

Soot emission to the atmosphere from vehicles, industrial machines, oil fires and others can add considerably to the Earth's energy budget and climate (Colbeck, Appleby, Hardman, & Harrison, 1990; Bergstrom, Russell, & Hignett, 2002; Chylek et al., 1996). On the other hand, soot exhaust can result in hazardous air pollution being a means for the transportation of semivolatile toxic combustion products. Soot particles (or aggregates of primary particles) of size 0.01–0.1 μm can penetrate and remain in the alveolar regions of the human lungs, causing local reactions, long-term chronic damage, resulting in mutagenic and carcinogenic effects (Koshland, 1996).

Most often soot is emitted to the atmosphere as aerosol aggregates composed of small primary particles (see, for example, Nyeki & Colbeck, 1995; Köylü, Mcenally, Rosner, & Pfefferle, 1997; Dobbins & Subramaniasivan, 1994). The morphology of the aggregates is a crucial factor which determines the transport of soot in the atmosphere, optical properties, efficiency to penetrate to the lungs of human and animals, and the aggregate surface area able to adsorb harmful combustion products. Soot aggregate morphology is controlled by different factors such as humidity (which leads to restructuring of aggregates to compact structures (Colbeck et al., 1990)), high temperature (which causes soot aggregate restructuring in the flame (di Stasio, 2001)) and electric charge on aggregates. The aggregate charge can effect the morphology at the stage of cluster–cluster aggregation (Richter, Sander, & Cheng, 1984; Hurd & Flower, 1988; Zhang, Sorensen, Ramer, Olivier, & Merklin, 1988; Julien & Meakin, 1989; Park, Kim, & Chang, 2001), and, besides, the charge can govern the aggregate restructuring resulting in transformation of chain-like structures to compact ones (Onischuk et al., 2003). It is known also that the lung deposition of inhaled aerosol may be significantly enhanced by the electric charges carried by particles (or aggregates of particles) (Vincent, 1985).

Thus, the electric charge of soot aggregates is an important parameter which affects the aggregate morphology and other properties. It was shown (see, for example, Place & Weinberg, 1966; Ball & Howard, 1971; Wersborg, Howard, & Williams, 1973; Onischuk et al., 2003; Burtscher, Reist, & Schmidt-Ott, 1986; Roth & Hospital, 1994; Popovicheva, Persiantseva, Starik, & Loukhonitskaya, 2003; Sorokin, Vancassel, & Mirabel, 2003) that soot aggregates formed in combustion are charged as well as flame generated inorganic aggregates (see, for example, Katzer, Weber, & Kasper, 2001). The soot aggregate charge arises from bipolar ion diffusion in the reaction zone (Calcote, 1981; Calcote & Gill, 1994; Burtscher et al., 1986; Rogak & Flagan 1992; Wen, Reischl, & Kasper, 1984a; Alonso, Hashimoto, Kousaka, Higuchi, & Nomura, 1998; Fuchs, 1964). It seems to be evident that the study of charge distribution for soot aggregates synthesized through different combustion and pyrolysis routes is important.

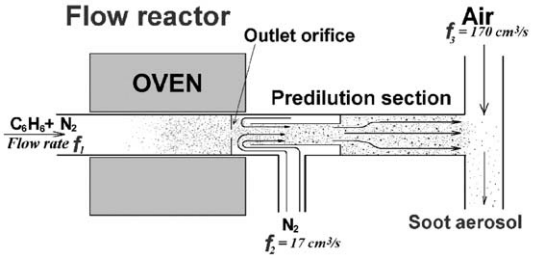

Fig. 1. Scheme of flow reactor.

Many particles present in the atmosphere, including soot, experience a force when exposed to visible light which causes them to migrate towards or away from the light source. This phenomenon is termed photophoresis. There is no unique opinion with regard to the role of photophoresis in vertical transport of soot in the atmosphere. The results of Kerker and Cooke (1982) suggest that the sun photophoresis force is not more than a few percent of the gravity force in the free-molecular region. However, Orr and Keng (1964) state that small particles may be very significantly influenced by the action of light in the stratosphere. Lewittes and Arnold (1982) concluded that 1 μm particles having particular dielectric and thermal properties should be levitated in the upper atmosphere by the ambient light. The recent estimations by Tehranian, Giovane, Blum, Xu, and Gustafson (2001) and Beresnev, Kovalev, and Kochneva (2003) predict the strong influence of sun photophoresis on vertical transport of soot particles at high altitudes. Besides, the numerical results of Mackowski (1989) indicate that photophoresis can be a significant transport mechanism for micrometer-sized particulates in high radiative transfer combustion environments. Thus, further theoretical and experimental studies of the role of photophoretic forces in the atmospheric particle transport, combustion and other processes are necessary.

This work deals with soot aggregates formed by benzene pyrolysis and propane combustion. Benzene is of interest, because the modern use of fuels with increased aromatic contents has increased particulate emissions from vehicular exhausts and industrial processes with regard to the fuels with low C/H ratio. On the other hand, propane is an important practical fuel and its combustion is characterized by the rapid decomposition into smaller intermediates C_1–C_3 which is similar to the combustion of more complex hydrocarbon fuels (Leung, Lindstedt, & Jones, 1993). That is why propane is often used for laboratory studies of combustion processes and, particularly, soot formation mechanisms.

This paper is aimed at a video and transmission electron microscopy (TEM) study of charged soot aggregates formed in both benzene pyrolysis and propane combustion. Charge distributions and photophoretic movement of these aggregates are investigated.

2. Experimental

Soot was generated by both benzene pyrolysis in a flow reactor and combustion in propane/air diffusion flame. In the case of the pyrolytic route of synthesis a mixture of benzene with nitrogen is supplied to the input of flow reactor (Fig. 1) at atmospheric pressure and room temperature. The partial pressure of benzene in the input mixture is 90 Torr. The majority of experiments were carried

out at a temperature of 1350 K in reaction zone. Therefore, when not mentioned specially, the reactor temperature should be implied as this. The input flow rate is varied in the range $f_1 = 0.25$–2.5 cm^3/s at STP which corresponds to the residence time in the reaction zone $t = 0.6$–6 s. There is an orifice of diameter 0.2 cm at the end of reaction zone. At the outlet of this orifice the outcoming flux is mixed with a cold nitrogen supplied with flow rate of $f_2 = 17$ cm^3/s (predilution). Downstream the soot aerosol is diluted again with a flux of air $f_3 = 170$ cm^3/s to suppress coagulation. The coagulation time in the predilution section is 3 s. The soot mass concentration in the flow is determined by deposition to a high efficiency Petrianov aerosol filter (Kirsch, Stechkina, & Fuchs, 1975).

Soot formed in a propane/air diffusion flame (Onischuk et al., 2003) was also analysed. A cylindrical burner with an inner diameter of 1 cm was fed with propane fuel (90% C_3H_8 + 7% C_4H_{10} + 3% CH_4 and C_2H_6) at flow rate of 5 cm^3/s at STP. The length of the visible part of the flame was about 22 cm. To avoid the influence of air fluctuations the flame was shielded by a co-annular cylindrical iron grid of diameter 7 cm. Soot aerosol for analysis was sampled both from the flame axis at different heights h above burner and from the region over the flame at $h = 27$ cm. When sampling from the flame axis the soot aerosol was sucked through a nickel capillary (i.d. = 1 mm, length = 6 cm) at 2 cm^3/s at STP at different heights above the burner. At the outlet of the capillary the flux was diluted 70 times by air. Then the diluted aerosol passed through an aerosol duct to the optical cell for video observations (see later the description of video system). The residence time in the capillary was about 20 ms, the residence time in the aerosol duct was 10 s. When sampling from the region over the flame the aerosol was sucked with the flow rate of 2.5 cm^3/s at STP through an aerosol duct directly to the optical cell. In this case the residence time in the duct was 23 s.

Size and shape of soot particles were analysed by a TEM. Soot particles were sampled thermophoretically from the flux to an electron microscopy greed covered by a polyvinylformvar film.

A microscopic video system was used for soot observations. Soot aerosol was injected to an optical cell at atmospheric pressure and room temperature. A focused He–Ne laser beam passed through the cell volume. Light scattered by aerosol particles at the angle of 90° passed through a flat window to the microscope objective and then to a CCD camera connected to the video system. The objective drew an image of particles presented in the illuminated volume of cell on the light-sensitive CCD matrix with a magnification of 15 times. The visualization field in the optical cell was near 300×400 μm^2. The focal depth in the object space is about 30 μm. The spatial resolution of the system was near 3 μm that allowed to obtain resolved images of aggregates larger than 3 μm. For smaller sizes, the aggregates were visible as spots. To create a homogeneous electric field, two parallel electrodes were fixed in the cell. The distance between electrodes was 0.25 cm. The movement of the aggregates in the electric field gave an information on the electric charge of aggregates.

3. Results

3.1. Soot aggregate size and morphology

TEM images showed that soot was forming as aggregates composed of small primary particles (Fig. 2a, b). The typical diameter of primary particles was 10–30 nm for the aggregates formed in the flame and 40–200 nm for the aggregates from flow reactor.

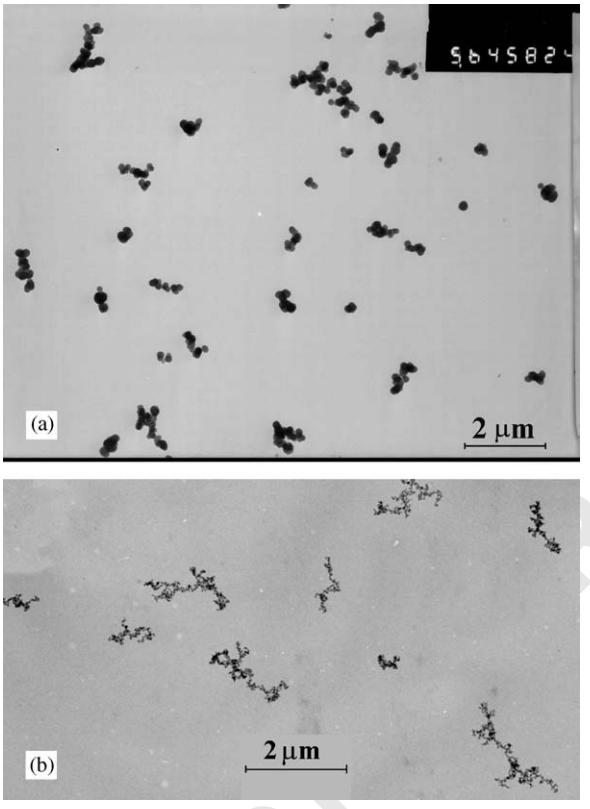

Fig. 2. TEM image of soot aggregates sampled from the flow reactor at input flow rate $f_1 = 1.4$ cm^3/s at SPT (a), and propane flame (from the region over the flame, height above burner $h = 27$ cm) (b).

Using the TEM images the radius of aggregates was measured as

$$R = \frac{1}{2}\sqrt{LW}, \tag{1}$$

where L and W are the dimensions of the smallest rectangle enclosing the image of single particles or aggregate. Fig. 3a shows frequency distribution of aggregate radius for soot formed by benzene pyrolysis at the input flow rate $f_1 = 0.8$ cm^3/s. Fig. 4 (circles) illustrates how the arithmetic mean radius of aggregates varies with input flow rate. One can see an increase of aggregate radius as the input flow rate increases. This increase of the aggregate radius is related to the increase of soot mass concentration in the predilution section (see Fig. 1).

We described the aggregate morphology in terms of fractal-like dimension D_f which can be determined from a power relation between the mass M of each aggregate and its radius R measured by TEM analysis (Friedlander, 2000):

$$M \propto R^{D_f}. \tag{2}$$

To determine D_f the values of aggregate masses were plotted as $\log M$ vs. $\log R$. To determine the aggregate mass (in arbitrary units) we measured the integral density of individual aggregate TEM

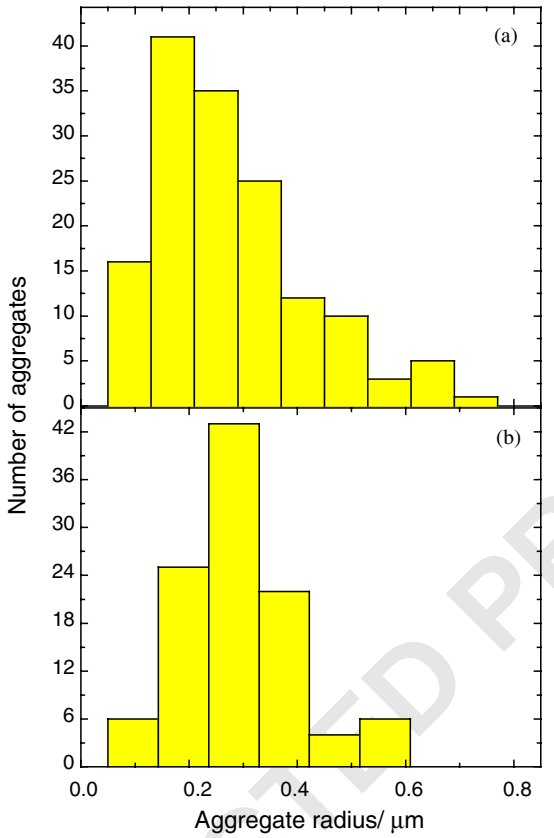

Fig. 3. Frequency distributions of aggregate radius. Soot aggregates were formed by benzene pyrolysis. Input flow rate $f_1 = 0.8$ cm^3/c: (a) TEM data; (b) data of video observation of Brownian motion.

image. The procedure was as follows. The image was elaborated as a file in format "bmp". The integral density was determined as the sum of the gray values of all the pixels which constituted the aggregate image. A correction to the background density was also done. It is assumed that the local density in the aggregate image is proportional to the local thickness of the original aggregate. Therefore, the mass of the original aggregate is considered to be proportional to the integral density of the aggregate image. This approach seems to be reasonable because it is known that even the fractal-like dimension of two-dimensional projection is approximately equal to the D_f value of the original 3D object if $D_f < 2$ (Friedlander, 2000; Rogak, Baltensperger, & Flagan, 1991). In case of soot formed by benzene pyrolysis we found that the fractal dimension does not depend on the input flow rate, being equal to (D_f=)1.8. Fig. 5 gives an example of $\log M$ vs. $\log R$. The fractal dimension for aggregates sampled from the region over the flame was also (D_f=)1.8.

Fig. 6 shows fraction of carbon from the initial benzene converted to soot which was determined as the ratio of soot mass concentration at the reactor outlet orifice to the mass concentration of carbon in benzene at the input. As mentioned above the majority of the results was obtained for the reactor temperature equal to 1350 K. Therefore it is interesting to compare the benzene to soot

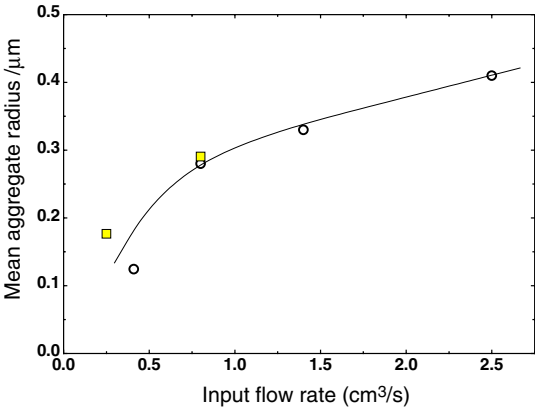

Fig. 4. Arithmetic mean radius of soot aggregates vs. input flow rate. Circles—TEM data; squares—data from the video observations of the aggregate Brownian motion. Soot aggregates were formed by benzene pyrolysis. Line is smooth fit through data.

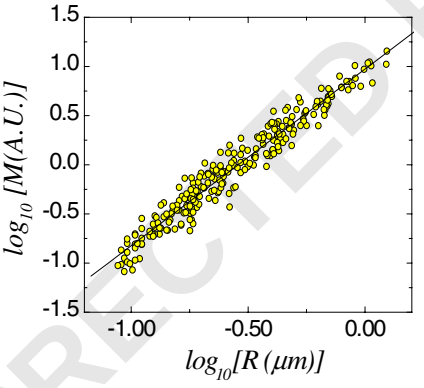

Fig. 5. Soot aggregate mass vs. radius. TEM data. Soot was formed by benzene pyrolysis at input flow rate $f_1 = 2.5$ cm^3/s. Solid line corresponds to fractal-like dimension $D_f = 1.8$.

conversion with the benzene decomposition degree ξ for this temperature:

$$\xi = 1 - [C_6H_6]/[C_6H_6]_0, \tag{3}$$

where $[C_6H_6]$ and $[C_6H_6]_0$ are benzene concentrations at the outlet orifice and inlet of reactor, respectively. For the input flow rate $f_1 = 0.67$ cm^3/s (corresponding to Fig. 6) we have the reaction time determined from the reactor temperature profile as $t = 2.3$ s. The effective first-order rate constant k_p of benzene pyrolysis was determined experimentally by Laskin and Lifshitz (1996) for a temperature $T = 1350$ K as equal to $k_p = 0.4$ s^{-1}. Thus, we can estimate the benzene decomposition degree:

$$\xi = 1 - \exp(-k_p t) = 0.6, \tag{4}$$

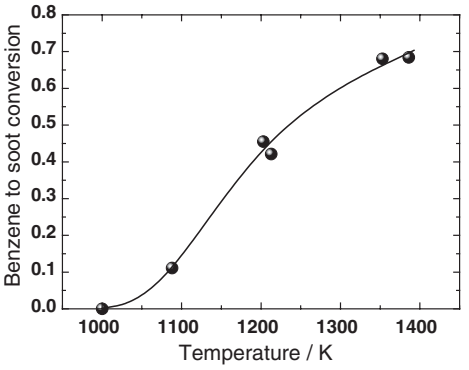

Fig. 6. Fraction of carbon from the initial benzene converted to soot vs. reactor temperature. Input flow rate $f_1 = 0.67$ cm^3/s. Conversion was estimated as ratio of soot mass concentration at the outlet of reactor to the input mass concentration of carbon to be a constituent of benzene. Line is smooth fit through data.

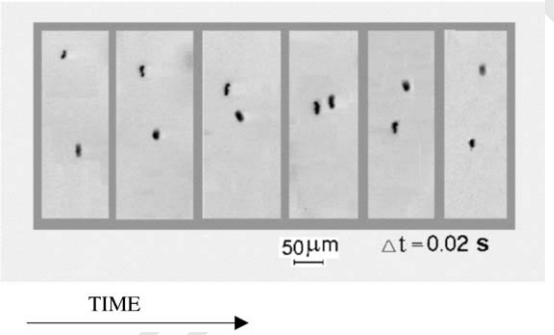

Fig. 7. A sequence of frames demonstrating movement of two charged aggregates in the electric field of 360 V/cm. The aggregates were formed in the benzene flow reactor.

which is equal to the benzene to soot conversion (Fig. 6) within the accuracy of 10%. In other words, the comparison of these estimation results with the experimentally measured benzene to soot conversion shows that the majority of decomposed benzene has converted to soot particles.

3.2. Video observations of soot aggregates

Movement of soot aggregates in the optical cell under a homogeneous electric field applied with a strength of 360 V/cm was studied using a video system. Fig. 7 gives an example of movement of two aggregates in the electric field. One can see that one of two aggregates moves downwards (negative charge), while the other aggregate moves upwards (positive charge). We estimated the aggregate net charge from the balance between the Coulomb force and the drag force F_D:

$$n_c e E = F_D, \tag{5}$$

where n_c is the number of the elementary charges on the aggregate, e the elementary charge (4.8×10^{-10} units of CGSE) and E the electric field strength. The drag force

$$F_D = \frac{6\pi v \eta R_m}{C_C}, \tag{6}$$

where η is the viscosity coefficient for air, v is the aggregate velocity, R_m is the mobility equivalent radius, C_C is Cunningham correction factor given (see, for example, Reist, 1993):

$$C_C = 1 + \frac{\lambda}{R_m}\left[A + Q\exp\left(-\frac{bR_m}{\lambda}\right)\right], \tag{7}$$

where $A = 1.26$, $Q = 0.40$, $b = 1.10$ and λ is the gas mean free path.

Thus, the charge of each aggregate was determined using Eqs. (5) and (6). The crucial point in these estimations was determination of R_m. Two different approaches were applied. In the first approach, the mobility equivalent radius of each aggregate was derived from the observation of it's Brownian motion without an electric field. The aggregate diffusion coefficient D was determined from the Einstein equation:

$$\overline{(\Delta x)^2} = 2D\tau, \tag{8}$$

$$\overline{(\Delta x)^2} = \frac{\Delta x_1^2 + \Delta x_2^2 + \cdots + \Delta x_N^2}{N},$$

where $\Delta x_1, \Delta x_2, \ldots, \Delta x_N$ are successive displacements of the aggregate along the horizontal x-axis over time interval $\tau = 0.8$ s. Then the equivalent mobility radius was derived from the expression for the diffusion coefficient:

$$D = \frac{k_B T C_C}{6\pi R_m \eta}, \tag{9}$$

where k_B is the Boltzmann constant and T is temperature. After recording the aggregate Brownian motion the electric field was switched on to measure the velocity of aggregate movement due to an electric force. This approach resulted in a charge distribution for the aggregates as presented in Fig. 8a. Fig. 3b demonstrates the frequency distribution of equivalent mobility radius determined by video observation of aggregate Brownian motion for the input flow rate $f_1 = 0.8$ cm^3/s. There is reasonable agreement between the radius distribution histograms determined by video observation and TEM image analysis (Fig. 3a) for this flow rate $f_1 = 0.8$ cm^3/s. Fig. 4 compares TEM and video data for the mean aggregate radius vs. input flow rate. The video observation overestimates the mean aggregate radius at $f_1 = 0.25$ cm^3/s with regard to the TEM data. The reason for this overestimation is fact that sensitivity limit of the video system approximately equal to ~ 0.1 μm. At $f_1 = 0.8$ cm^3/s there is satisfactory agreement between video and TEM data. Therefore, we assume that the video system gives reasonable values of the mean mobility radius at $f_1 > 0.5$ cm^3/s. In the second approach the same average radius was used to characterize each aggregate recorded by the video system. This average R was determined by elaboration of TEM images. Fig. 8b shows the frequency distribution of aggregate charge for this way of data treatment. One can see a good agreement between the two histograms obtained from TEM image elaboration (Fig. 8b) and video observations of Brownian motion (Fig. 8a) indicating the validity of both ways of aggregate charge distribution measurement. Figs. 8a, b show that there is approximately a symmetric bipolar charge distribution of soot aggregates. The typical aggregate net charge is a few elementary units.

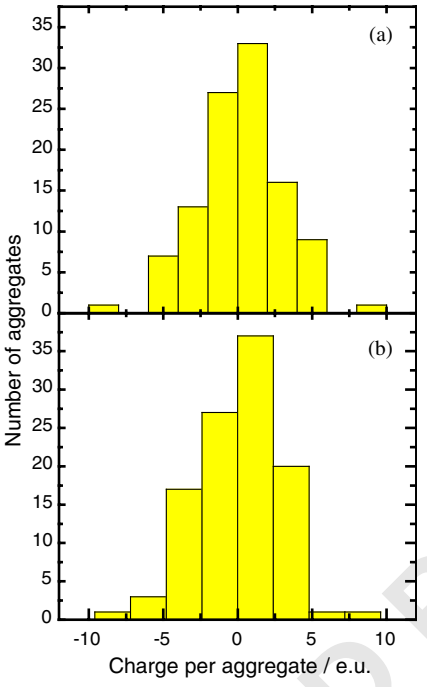

Fig. 8. Frequency distribution of aggregate charge determined by video observations. Soot was formed by benzene pyrolysis at input flow rate $f_1 = 0.8$ cm^3/c. When estimating charge the aggregate radius was determined: (a) for each aggregate by video registration of Brownian motion and (b) by elaboration of TEM data (the same average radius was used for each aggregate).

Fig. 9 presents a scattering plot in coordinates aggregate charge–mobility radius. One can see that the greater the aggregate radius the wider the charge distribution.

Video observations showed that soot aggregates illuminated by the light of He–Ne laser moved in the direction of the beam due to photophoresis. For each aggregate observed by the video system we determined both photophoretic velocity (at the power of light beam of 3 W/cm) and equivalent radius (by Brownian motion for small aggregates or settling velocity for large ones). We found that the photophoretic velocity increased with the equivalent radius. To demonstrate the dependence of photophoretic velocity on equivalent radius we divided the experimental points into several groups, uniting the points of neighbouring radii in one group and averaging photophoretic velocities and equivalent radii in each group. Fig. 10a demonstrates this dependence of photophoretic velocity on radius. It is worth to say separately about the procedure of equivalent radius determination from the settling velocity. It was possible to observe both random Brownian motion (which gave mobility radius R_m) and settling motion for relatively small aggregates. For these aggregates, we can estimate the mass from the balance between drag force and gravity force,

$$\frac{6\pi v_{settl}\eta R_m}{C_C} = Mg, \tag{10}$$

where g is the acceleration due to gravity and v_{settl} is the settling velocity. Assuming the aggregate fractal dimension $D_f = 1.8$ (see Fig. 5), we can estimate equivalent mobility radius from the settling

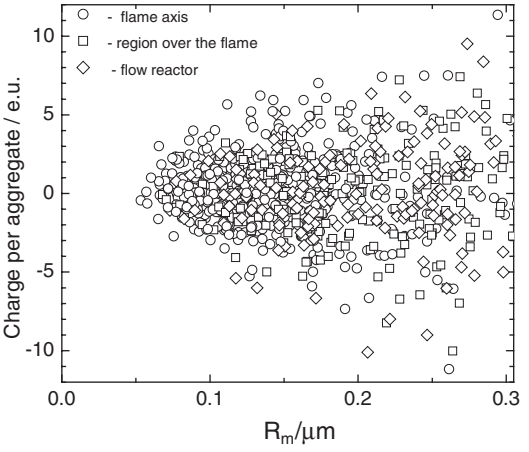

Fig. 9. Scattering graph in coordinates mobility radius—net aggregate charge. Mobility radius for each aggregate was determined by the video observation of Brownian motion. Points for soot formed by benzene pyrolysis (at the input flow rates $f_1 = 0.25$ and 0.8 cm^3/s) and propane combustion sampled from the flame axis (at height above burner $h = 5.5$, 7.8, 10.0 and 13.3 cm) and from the region over the flame at $h = 27$ cm are put in the same graph.

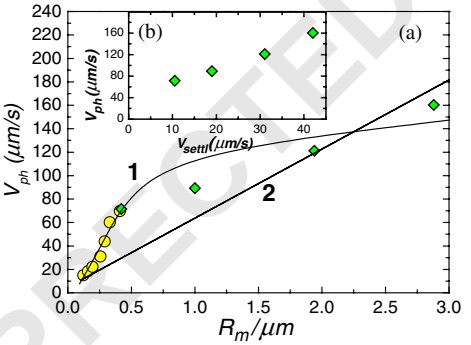

Fig. 10. (a) Aggregate photophoretic velocity vs. mobility equivalent radius of aggregates. R_m was determined by Brownian (circles) and settling motion (diamonds). (b) shows photophoretic velocity vs. settling velocity. Solid lines are estimations of aggregate photophoretic velocity: 1—Eq. (14) (single particle approximation); 2—Eq. (18) (ensemble of primary particles approximation).

velocity of larger aggregates (for which the Brownian movement is negligible) solving Eq. (10) with

$$M = M_0 \left(\frac{R_m}{R_m^0} \right)^{D_f}, \tag{11}$$

where R_m^0 and M_0 are mobility radius and mass of relatively small aggregate determined via observation of Brownian motion and gravitional settling, respectively; M is the mass of large aggregate and R_m is mobility radius of large aggregate. The diamond points in Fig. 10a are calculated via Eqs. (10) and (11).

4. Discussion

4.1. Steady-state charge distribution

Aerosol particles in a bipolar ion atmosphere come to a steady-state condition. For particles larger than 0.05 μm the distribution of charges at the steady-state condition corresponds to the dynamic electrical equilibrium described by the Boltzmann law (see, for example, Hussin, Scheibel, Becker, & Porstendorfer, 1983; Liu & Pui, 1974; Wen, Reischl, & Kasper, 1984a, b; Fuchs, 1964):

$$f(q) = \frac{1}{\sum} \exp\left(-\frac{(q)^2}{d_E k_B T}\right), \tag{12}$$

$$\sum = \sum_{-\infty}^{\infty} \exp\left(-\frac{(q)^2}{d_E k_B T}\right), \tag{13}$$

where $f(q)$ is the fraction of particles which have the charge q, k_B is Boltzmann constant, T is temperature and d_E is the charging equivalent diameter. It was shown by Rogak et al. (1991) and Wen et al. (1984b) that the steady-state charging equivalent diameter for aggregates in bipolar ionic atmosphere is approximately equal to the aggregate mobility diameter.

Fig. 9 shows a scattering plot in coordinates aggregate charge–equivalent mobility radius for the soot aggregates of three kinds: sampled from the flame axis, from the region over the flame and from the flow reactor. For each kind of aggregates it is possible to select a narrow range of radius in this charge–radius diagram. In this case, we have the charge distribution for the selected range of radius. Fig. 11 demonstrates a charge distribution for soot aggregates sampled from the axis of flame with the aggregate diameter being in the range 0.20–0.25 μm. This charge distribution can be fitted by the Gaussian function (12) for room temperature and $d_E = 0.35$ μm. This charging equivalent diameter d_E exceeds the average mobility diameter $d_m = 0.23$ μm. In other words, the charge distribution for these soot aggregates is wider than equilibrium being intermediate between flame temperature and room temperature equilibrium. Fig. 12 shows d_E versus d_m for soot aggregates generated in different conditions demonstrating that the charge distributions for all the three types

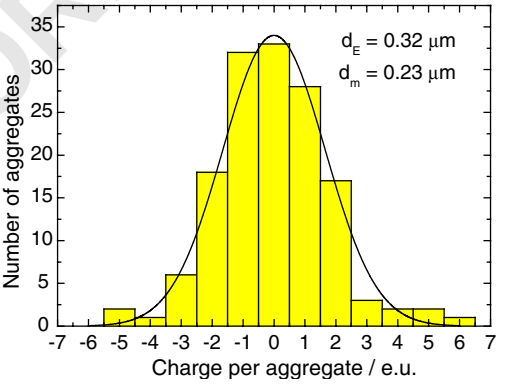

Fig. 11. Frequency distribution of aggregate net charge. The range of aggregate mobility diameter is 0.20–0.25 μm. Aerosol was sampled from the flame axis. Solid line is governed by the Boltzmann equation (12) with a charging equivalent diameter $d_E = 0.32$ μm. Mean arithmetic mobility diameter is 0.23 μm.

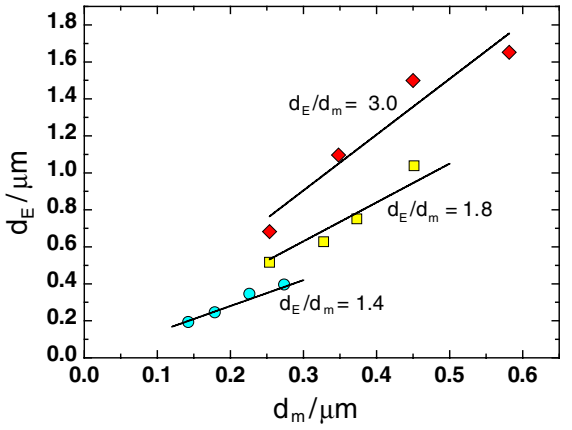

Fig. 12. Charging equivalent diameter d_E versus mobility equivalent diameter d_m for the data presented in Fig. 9. Soot was sampled from the flame axis (circles), region over the flame (diamant), and from the flow reactor (squares). Solid lines correspond to linear functions $d_E = 3.0d_m$; $d_E = 1.8d_m$; $d_E = 1.4d_m$.

of soot aggregates are wider than equilibrium distributions. Thus, we can conclude that there is an over-equilibrium charge distribution of soot aggregates sampled both from the flame and from the flow reactor. It is appropriate to mention that Burtscher et al. (1986) have also registered aerosol particle charge above equilibrium at room temperature for soot formed by open fires of hydrocarbons.

Let us discuss now some details of the over-equilibrium charge spectrum formation. Combustion and pyrolysis of hydrocarbons are characterized by a high ion concentration. Thus, the ion concentration is 10^8–10^{11} cm^3 in the flame (Calcote, 1981; Calcote & Gill, 1994; Lewis & Von Elbe, 1961) and up to 10^{15} cm^{-3} in thermal decomposition processes (Calcote, 1981). Simple estimations of charging kinetics by the collision theory show that the charge distribution on soot particles in the flame is equilibrium. When increasing distance from the reaction zone both temperature and ion concentration drops down. Therefore, the soot charge distribution becomes wider than the equilibrium distribution for this decreased temperature. The subsequent coagulation of soot aerosol is characterized by two opposite tendencies. One tendency is charge spectrum broadening due to random coagulation, the other one is aggregate charge limitation due to Coulomb interaction between colliding aggregates. It is evident that at the room temperature the second tendency of charge limitation due to Coulomb interaction is predominant resulting in more narrow charge spectrum than the flame temperature equilibrium distribution. On the other hand, this resulting spectrum is still wider than the room temperature equilibrium distribution.

4.2. Photophoresis

Fig. 10 demonstrates the photophoretic velocity of aggregates vs. aggregate mobility radius. One can see a monotonic increase of photophoretic velocity with equivalent mobility radius. To explain this monotonic increase we estimated the photophoretic velocity as function of aggregate radius. Two approaches were applied. In the first approach, we considered the aggregate as a single particle. In the case of a single spherical particle of radius r the photophoretic velocity can be estimated via the

expression (Beresnev et al., 2003)

$$V_{\mathrm{Ph}}^{\mathrm{single}} = -\frac{\pi}{2(8+\pi)}\,\frac{IJ_1}{p_0}\,\frac{\psi_1}{\psi_3(1+(\chi_i/\chi_a)\psi_2)}, \tag{14}$$

where ψ_1, ψ_2 and ψ_3 are functions dependent only on Kn number ($Kn = \lambda/r$):

$$\psi_1 = \frac{Kn}{Kn+\frac{5\pi}{18}}\left(1+\frac{2\pi^{0.5}Kn}{5Kn^2+\pi^{0.5}Kn+\pi/4}\right),$$

$$\psi_2 = \left(0.5+\frac{15}{4}\,Kn\right)\left(1-\frac{1.21\pi^{0.5}Kn}{100Kn^2+\pi/4}\right),$$

$$\psi_3 = \frac{Kn}{Kn+0.619}\left(1+\frac{0.31Kn}{Kn^2+1.152Kn+0.785}\right), \tag{15}$$

p_0 is the ambient gas pressure (equal to atmospheric pressure 1.01×10^6 dyne/cm^2), I the intensity of light (erg cm^{-2} s^{-2}), J_1 the so-called photophoretic asymmetry factor depending on the particle radius and illuminating light wavelength, λ is mean free pass for gas molecules, χ_a and χ_i are coefficients of thermal conductivity for gas ($\chi_a = 2.4\times10^3$ erg/(cm s K)) and material of particle, respectively.

In the second case, we considered the aggregate as an ensemble of primary particles. The photophoretic force $F_{\mathrm{Ph}}^{\mathrm{agg}}$ acting to an aggregate was assumed to be equal to the sum of forces acting on primary particles. The force acting on a primary particle of radius r can be estimated via expression (Chernyak & Beresnev, 1993)

$$F_{\mathrm{Ph}}^{\mathrm{single}} = -\frac{\pi}{3}\,r^2 IJ_1\left(\frac{\pi m}{2k_{\mathrm{B}}T}\right)^{0.5}\frac{\psi_1}{1+(\chi_i/\chi_a)\psi_2}. \tag{16}$$

We can estimate the equivalent number of illuminated primary particles in the aggregate as R_a/r^2, where R_a is the radius of spherical particle with projected area equal to the projected area of aggregate. Thus, the aggregate photophoretic force is given by

$$F_{\mathrm{Ph}}^{\mathrm{agg}} = F_{\mathrm{Ph}}^{\mathrm{single}}(R_a/r)^2. \tag{17}$$

It was shown by Rogak et al. (1993) that the equivalent mobility radius R_m is approximately equal to the mean projected area radius R_a. Therefore, from Eqs. (16), (17) we estimate:

$$F_{\mathrm{Ph}}^{\mathrm{agg}} = -\frac{\pi}{3}\,IJ_1\left(\frac{\pi m}{2k_{\mathrm{B}}T}\right)^{0.5}R_{\mathrm{m}}^2\,\frac{\psi_1}{1+(\chi_i/\chi_a)\psi_2}. \tag{18}$$

The photophoretic velocity can be determined from the balance between the photophoretic force and drag force (6).

To estimate photophoretic velocity we need J_1. This asymmetry factor is calculated by Beresnev et al. (2003) for different values of real (n) and imaginary (k) parts of the soot refractive index and different values of the wavelength. It is known (see, for example, Chang & Charalampopoulos, 1990; Brewster, 1992) that in the range of wavelength 0.5–1.0 μm the real and imaginary parts of refractive index are most often in the ranges $1.7 < n < 2.0$ and $0.5 < k < 0.8$ for soot. Using the values of

J_1 from Beresnev et al. (2003) we estimated the aggregate photophoretic velocity for both single particle approximation and ensemble of primary particles approximation. Fig. 10a (curves 1 and 2) demonstrates the calculation results for $n = 1.95$ and $k = 0.8$. Both curves 1 and 2 (corresponding to the single particle and ensemble of particles approximations, respectively) were calculated for the thermal conductivity coefficient of soot particles $\chi_i = 4.3 \times 10^5$ erg/(cm s K). One can see that both curves 1 and 2 demonstrate the increase of photophoretic velocity with aggregate equivalent radius. For comparison, we calculated also photophoretic velocity for $n = 1.95$ and $k = 0.5$ (not shown in Fig. 10). These calculations gave $\chi_i = 3.6 \times 10^5$ erg/(cm s K) for the single particle approximation and $\chi_i = 2.0 \times 10^5$ erg/(cm s K) for the ensemble of particles approximation. The curves determined for these last values of the real and imaginary parts of refractive index were similar to the curves 1 and 2.

It is natural to expect that the estimated thermal conductivity coefficient for soot particles $\chi_i = (2–4) \times 10^5$ erg/(cm s K) lies between these coefficients for polyaromatic hydrocarbons and graphite which can be considered as soot precursors and the latest product in the soot formation process, respectively. Indeed, the thermal conductivity coefficients for naphthalene and graphite are 3.8×10^4 and $\sim 1 \times 10^7$ erg/(cm sK), respectively. Thus, one can see that soot thermal conductivity coefficient determined from estimations lies between these values for naphthalene and graphite in agreement with our previous assumption.

It seems interesting to compare the measured aggregate settling velocity with possible sun photophoretic velocity for these aggregates in the atmosphere at ground level. The sun constant is 1.368×10^6 erg/(cm^2 s) which is about 20 times less than our laser beam irradiation (3×10^7 erg/cm^2 s). Thus, we can expect that the sun photophoretic velocity V_{Ph}^{Sun} will be about 20 times less than the laser photophoresis values we measured in the laboratory. Therefore, from Fig. 10b we can see that V_{Ph}^{Sun} is about 20% of gravitional settling velocities.

Beresnev et al. (2003) have demonstrated by theoretical estimations that there can be a situation of soot particle levitation due to thermal irradiation of the Earth. These authors have shown that the upward photophoretic force is higher than the gravity force for soot particles of size about 1.5 μm. Therefore, we estimated the possible photophoretic contribution from thermal irradiation of the Earth to the vertical transport of our soot aggregates in the atmosphere. The intensity of this irradiation is about 4×10^5 erg/(cm^2 s) near the Earth's surface during the summer time (Anderson et al., 1986) which is 75 times less than our laser beam irradiation. The asymmetry factor J_1 for thermal irradiation of the Earth (the wavelength is ~ 10 μm) is about 6 times less than for He–Ne laser wavelength. Thus, based upon the data presented in Fig. 10b, we estimate the photophoretic velocity from the Earth irradiation to be about 1% of the settling velocity for the soot aggregates studied in this paper.

5. Conclusions

By means of the video observation, charge distributions of soot aggregates synthesized by propane combustion and benzene pyrolysis were determined. The charge distribution of soot aggregates is above equilibrium being larger than room temperature equilibrium by a factor of 1.4, 3.0 and 1.8 for soot sampled from the flame axis, region over the flame and from the flow reactor, respectively.

Measurements of the aggregate photophoretic velocity as a function of equivalent mobility radius were done for soot aggregates formed by benzene pyrolysis. The aggregate photophoretic velocity was found to be increasing from 15 to 160 μm/s with the equivalent radius increasing from 0.1 to 2.9 μm. Estimations of sun photophoretic velocities $V_{\mathrm{Ph}}^{\mathrm{Sun}}$ (in the Earth's atmosphere at ground level) were performed in comparison with the aggregate settling velocity. These estimations testified that $V_{\mathrm{Ph}}^{\mathrm{Sun}}$ is about 20% of settling velocity for the range of aggregate radii studied in this work. The Earth radiation photophoresis velocity was estimated to be negligible with regard to the settling velocity of soot aggregates.

Acknowledgements

The authors would like to gratefully acknowledge the financial supports provided by *INTAS foundation* (*Grant 2000-00460*), *Russian Foundation for Basic Research* (*project 01-03-32390*), *and grant of ISTC No. 2358.*

References

Alonso, M., Hashimoto, T., Kousaka, Y., Higuchi, M., & Nomura, T. (1998). Transient bipolar charging of a coagulating nanometer aerosol. *Journal of Aerosol Science*, *29*, 263–270.

Anderson, G. P., Clough, S. A., Kneizys, F. X. et al. (1986). AFGL Atmospheric Constituent Profiles (0–120 km). Air Force Geophysic Laboratory (USA): AFGL-TR-0110, ERP No. 954, 43p.

Ball, R. T., & Howard, J. B. (1971). Electric charge of carbon particle in flames: *13th international symposium on combustion*, Vol. 353, The Combustion Institute.

Beresnev, S. A., Kovalev, F. D., & Kochneva, L. B., et al. (2003). On the possibility of particle's photophoretic levitation in the stratosphere. *Atmospheric Oceanic Opt.*, *16*(1), 44–48.

Bergstrom, R. W., Russell, P. B., & Hignett, P. (2002). On the wavelength dependence of the absorption of black carbon particles: Predictions and results from the TARFOX experiment and implications for the aerosol single scattering albedo. *Journal of Atmospheric Science*, *59*(3., Pt. 1), 567–577.

Brewster, M. Q. (1992). *Thermal radiative transfer and properties*. New York/Chichester/Brisbane/Toronto/Singapore: Wiley.

Burtscher, H., Reist, A. R., & Schmidt-Ott, A. (1986). Particle charge in combustion aerosols. *Journal of Aerosol Science*, *17*, 47–51.

Calcote, H. F. (1981). Mechanism of soot nucleation in flames—a critical review. *Combustion and Flame*, *42*, 215–242.

Calcote, H. F., & Gill, R. J. (1994). Comparison of the ionic mechanism of soot formation with a free radical mechanism. In H. Bockhorn (Ed.), *Soot formation in combustion* (pp. 471–482). Berlin: Springer.

Chang, H., & Charalampopoulos, T. T. (1990). Determination of the wavelength dependence of refractive indices of flame soot. *Proc. R. Soc. Lond. A*, *430*, 577–591.

Chernyak, V., & Beresnev, S. (1993). Photophoresis of aerosol particles. *Journal of Aerosol Science*, *24*, 857–866.

Chylek, P., Lesins, G. B., Videen, G., Wong, J. G. D., Pinnick, R. G., Ngo, D., & Klett, J. D. (1996). Black carbon and absorption of solar radiation by clouds. *Journal of Geophysical Research*, *101*(D18), 23,365–23,371.

Colbeck, I., Appleby, L., Hardman, E. J., & Harrison, R. M. (1990). The optical properties and morphology of cloud-processed carbonaceous smoke. *Journal of Aerosol Science*, *21*, 527–538.

di Stasio, S. (2001). Observation of restructuring of nanoparticle soot aggregates in a diffusion flame by static light scattering. *Journal of Aerosol Science*, *32*, 509–524.

Dobbins, R. A., & Subramaniasivan, H. (1994). Soot precursor particles in flames. In H. Bockhorn (Ed.), *Soot formation in combustion* (pp. 290–301). Berlin: Springer.

Friedlander, S. K. (2000). *Smoke, dust, and haze*. New York, Oxford: Oxford University Press.

Fuchs, N. A. (1964). *The mechanics of aerosols*. Oxford: Pergamon Press.

Hurd, A. J., & Flower, W. L. (1988). In situ growth and structure of fractal silica aggregates in a flame. *Journal of Colloid and Interface Science*, *122*, 178–192.

Hussin, A., Scheibel, H. G., Becker, K. H., & Porstendorfer, J. (1983). Bipolar diffusion charging of aerosol particles—I: Experimental results within the diameter range 4–30 nm. *Journal of Aerosol Science*, *14*, 671–677.

Julien, R., & Meakin, P. (1989). Simple models for the restructuring of three-dimensional ballistic aggregates. *Journal of Colloid and Interface Science*, *127*, 265–272.

Katzer, M., Weber, A. P., & Kasper, G. (2001). The effects of electric fields on growth of titania particles formed in CH_4–O_2 diffusion flame. *Journal of Aerosol Science*, *32*, 1045–1067.

Kerker, M., & Cooke, D. D. (1982). Photophoretic force on aerosol particles in the free-molecule regime. *Journal of the Optical Society of America*, *72*, 1267–1272.

Kirsch, A. A., Stechkina, I. B., & Fuchs, N. A. (1975). Efficiency of aerosol filters made of ultrafine polydisperse fibres. *Journal of Aerosol Science*, *5*, 119–124.

Koshland, C. P. (1996). Impacts and control of air toxics from combustion. *26th symposium* (*international*) *on combustion*, pp. 2049–2065.

Köylü, Ü. O., Mcenally, C. S., Rosner, D. E., & Pfefferle, L. D. (1997). Simultaneous measurements of soot volume fraction and particle size/microstructure in flames using a thermophoretic sampling technique. *Combustion and Flame*, *110*, 494–507.

Laskin, A., & Lifshitz, A. (1996). Thermal decomposition of benzene. Single-pulse shock tube investigation. *26th symposium* (*international*) *on combustion*, pp. 669–675.

Leung, K. M., Lindstedt, R. P., & Jones, W. P. (1993). Reduced kinetic mechanisms for propane diffusion flames. In N. Peters, & B. Rogg (Eds.), *Reduced kinetic mechanisms for application in combustion systems* (pp. 257–283). Berlin: Springer.

Lewis, B., & Von Elbe, G. (1961). *Combustion, flames and explosions of gases*. New York and London: Academic Press.

Lewittes, M., & Arnold, S. (1982). Radiometric levitation of micron sized spheres. *Applied Physics Letters*, *40*, 455–457.

Liu, B. Y. H., & Pui, D. Y. H. (1974). Electrical neutralization of aerosols. *Journal of Aerosol Science*, *5*, 465–472.

Mackowski, D. W. (1989). Photophoresis of aerosol particles in the free molecular and slip-flow regimes. *International Journal of Heat Mass Transfer*, *32*, 843–854.

Nyeki, S., & Colbeck, I. (1995). Fractal dimension analysis of single, in-situ, restructured carbonaceous aggregates. *Aerosol Science and Technology*, *23*, 109–120.

Onischuk, A. A., di Stasio, S., Karasev, V. V., Baklanov, A. M., Makhov, G. A., Vlasenko, A. L., Sadykova, A. R., Shipovalov, A. V., & Panfilov, V. N. (2003). Evolution of structure and charge of soot aggregates during and after formation in a propane/air diffusion flame. *Journal of Aerosol Science*, *34*, 383–403.

Orr Jr., C., & Keng, E. Y. H. (1964). Photophoretic effects in the stratosphere. *Journal of the Atmospheric Sciences*, *21*, 475–478.

Park, H., Kim, S., & Chang, H. (2001). Brownian dynamic simulation for the aggregation of charged particles. *Journal of Aerosol Science*, *32*, 1369–1388.

Place, E. R., & Weinberg, F. J. (1966). Electrical control of flame carbon. *Proceedings of the Royal Society, A*, *289*, 192–205.

Popovicheva, O. B., Persiantseva, N. M., Starik, A. M., & Loukhonitskaya, E. E. (2003). Ion–soot interaction: A possible mechanism of ion removal in aircraft plume. *Journal of Environmental Monitoring*, *5*, 265–268.

Reist, P. C. (1993). *Aerosol science and technology*. New York: McGraw-Hill.

Richter, R., Sander, L. M., & Cheng, Z. (1984). Computer simulations of soot aggregates. *Journal of Colloid and Interface Science*, *100*(1), 203–209.

Rogak, S. N., Baltensperger, U., & Flagan, R. C. (1991). Measurement of mass transfer to agglomerate aerosols. *Aerosol Science and Technology*, *14*, 447–458.

Rogak, S. N., & Flagan, R. C. (1992). Bipolar diffusion charging of spheres and agglomerate aerosol particle. *Journal of Aerosol Science*, *23*, 693–710.

Rogak, S. N., Flagan, R. C., & Nguyen, H. V. (1993). The mobility and structure of aerosol agglomerates. *Aerosol Science and Technology*, *18*, 25–47.

Roth, P., & Hospital, A. (1994). Mass growth of charged soot particles in premixed flames. In H. Bockhorn (Ed.), *Soot formation in combustion* (pp. 239–251). Berlin: Springer.

Sorokin, A., Vancassel, X., & Mirabel, P. (2003). Emission of ions and charged soot particles by aircraft engines. *Atmospheric Chemistry and Physics*, *3*, 325–334.

Tehranian, S., Giovane, F., Blum, J., Xu, Y. -L., & Gustafson, Bo. A. S. (2001). Photophoresis of micrometer-sized particles in the free-molecular regime. *International Journal of Heat Mass Transfer*, *44*, 1649–1657.

Vincent, J. H. (1985). On the practical significance of electrostatic lung deposition of isomeric and fibrous aerosols. *Journal of Aerosol Science*, *16*, 511–519.

Wen, H. Y., Reischl, G. P., & Kasper, G. (1984a). Bipolar diffusion charging of fibrous aerosol particles—I. Charging theory. *Journal of Aerosol Science*, *15*, 89–101.

Wen, H. Y., Reischl, G. P., & Kasper, G. (1984b). Bipolar diffusion charging of fibrous aerosol particles—II. Charge and electrical mobility measurements on linear chain aggregates. *Journal of Aerosol Science*, *15*, 103–122.

Wersborg, B. L., Howard, J. B., & Williams, G. C. (1973). Physical mechanisms in carbon formation in flames. *14th international symposium on combustion*, Vol. 929, The Combustion Institute.

Zhang, H. X., Sorensen, C. M., Ramer, E. R., Olivier, B. J., & Merklin, J. F. (1988). In situ optical structure factor measurements of an aggregating soot aerosol. *Langmuir*, *4*, 867–871.